

Molecular basis of ligand recognition and transport by glucose transporters

Dong Deng^{1,2,3*}, Pengcheng Sun^{1,2,3*}, Chuangye Yan^{1,2,3}, Meng Ke^{1,2,3}, Xin Jiang^{1,2}, Lei Xiong³, Wenlin Ren^{1,2}, Kunio Hirata^{4,5}, Masaki Yamamoto⁴, Shilong Fan² & Nieng Yan^{1,2,3}

The major facilitator superfamily glucose transporters, exemplified by human GLUT1–4, have been central to the study of solute transport. Using lipidic cubic phase crystallization and microfocus X-ray diffraction, we determined the structure of human GLUT3 in complex with D-glucose at 1.5 Å resolution in an outward-occluded conformation. The high-resolution structure allows discrimination of both α - and β -anomers of D-glucose. Two additional structures of GLUT3 bound to the exofacial inhibitor maltose were obtained at 2.6 Å in the outward-open and 2.4 Å in the outward-occluded states. In all three structures, the ligands are predominantly coordinated by polar residues from the carboxy terminal domain. Conformational transition from outward-open to outward-occluded entails a prominent local rearrangement of the extracellular part of transmembrane segment TM7. Comparison of the outward-facing GLUT3 structures with the inward-open GLUT1 provides insights into the alternating access cycle for GLUTs, whereby the C-terminal domain provides the primary substrate-binding site and the amino-terminal domain undergoes rigid-body rotation with respect to the C-terminal domain. Our studies provide an important framework for the mechanistic and kinetic understanding of GLUTs and shed light on structure-guided ligand design.

Cellular uptake of glucose is a fundamental process for metabolism, growth and homeostasis¹. The SLC2 family glucose transporters (GLUTs) catalyse facilitative diffusion of glucose and other monosaccharides across biomembranes^{2,3}. The fourteen human GLUTs have specific spatial and temporal distributions and exhibit distinct transport kinetics, capacity and substrate selectivity⁴.

GLUT1–4 are among the most rigorously characterized solute transporters. GLUT1, which was one of the first transporters to be characterized^{5–7}, has been a paradigm in the understanding of solute transport^{1,8}. GLUT1 is the principal glucose transporter in erythrocytes and blood-tissue barriers, and ubiquitous for basal-level glucose uptake^{9,10}. GLUT2 represents the major hepatocyte isoform that allows both uptake and efflux of glucose in response to fed or fasted state. GLUT2 also mediates glucose transport in intestinal, kidney and β -pancreatic cells^{11,12}. GLUT3 is referred to as the ‘neuronal glucose transporter’ for its primary function in neurons, and it is also responsible for glucose uptake in sperm, preimplantation embryos and circulating white blood cells¹³. GLUT4 is responsive to insulin in adipocytes and muscles^{14,15}.

Inactivating mutations or mis-regulations of GLUTs are associated with deleterious diseases including GLUT1 deficiency syndrome (the De Vivo disease), Fanconi–Bickel syndrome, type 2 diabetes mellitus and Alzheimer’s disease^{16–19}. GLUT1 and GLUT3 are overexpressed in different types of solid tumours, where the demand for glucose is strikingly enhanced to compensate for ATP generation under anaerobic conditions (the Warburg effect)^{20–24}. Targeting the overexpression of GLUTs for cancer diagnosis and potential therapy has drawn increasing attention²⁵, exemplified by the positron emission tomography that monitors the uptake of 2-deoxy-2-[¹⁸F]fluoroglucose^{1,26,27}. Glucose conjugations were designed to use glucose transporters for enhanced membrane permeation and tissue-specific delivery of anti-cancer

drugs²⁸. Structural determination of GLUTs, particularly in complex with ligands, is a prerequisite for ligand design and optimization.

GLUTs function by the ‘alternating access’ mechanism, whereby the alternate exposure of the substrate-binding site(s) to either side of the membrane is achieved through cycles of conformational changes of the transporter^{29–31}. The structure of GLUT1 was recently captured in an inward-open conformation³². Structures of Xyle, the *Escherichia coli* homologue of GLUTs, are available in three states: ligand-bound and outward-occluded³³, inward-open^{34,35}, and partly inward-occluded³⁴.

Here we present the *in meso* crystal structure of human GLUT3 bound to D-glucose in an outward-occluded state at 1.5 Å resolution. Structures of GLUT3 in complex with the exofacial competitive inhibitor maltose were also obtained in the outward-open and outward-occluded conformations. Structural comparison with the inward-open GLUT1 reveals the molecular basis for substrate recognition and transport by GLUTs.

Characterizations of the recombinant GLUT3(N43T)

All the functional and structural characterizations of GLUT3 reported here were performed using the glycosylation-site-eliminated variant GLUT3(N43T), which will be referred to as GLUT3 hereafter. A proteoliposome-based counterflow assay was reconstituted following a modified protocol^{36,37}, and the substrate selectivity of the recombinant GLUT3 was examined qualitatively (Fig. 1a, b). Among fifteen tested hexoses and pentoses, D-glucose, D-galactose, D-mannose, D-xylose and D-fucose blocked more than 90% of the [³H]glucose uptake, and L-arabinose and D-lyxose inhibited more than half of the activity. The other sugars had little or no effect on the transport. Notably, the C3 hydroxyl (C3-OH) of the seven effective inhibitors exhibits the same equatorial configuration, suggesting that C3-OH

¹State Key Laboratory of Membrane Biology, Tsinghua University, Beijing 100084, China. ²Center for Structural Biology, Tsinghua University, Beijing 100084, China. ³Tsinghua-Peking Center for Life Sciences, School of Life Sciences and School of Medicine, Tsinghua University, Beijing 100084, China. ⁴Advanced Photon Technology Division, Research Infrastructure Group, SR Life Science Instrumentation Unit, RIKEN/SPring-8 Center, 1-1-1 Kouto Sayo-cho Sayo-gun, Hyogo 679-5148 Japan. ⁵Precursory Research for Embryonic Science and Technology (PRESTO), Japan Science and Technology Agency, 4-1-8 Honcho, Kawaguchi, Saitama 332-0012, Japan.

*These authors contributed equally to this work.

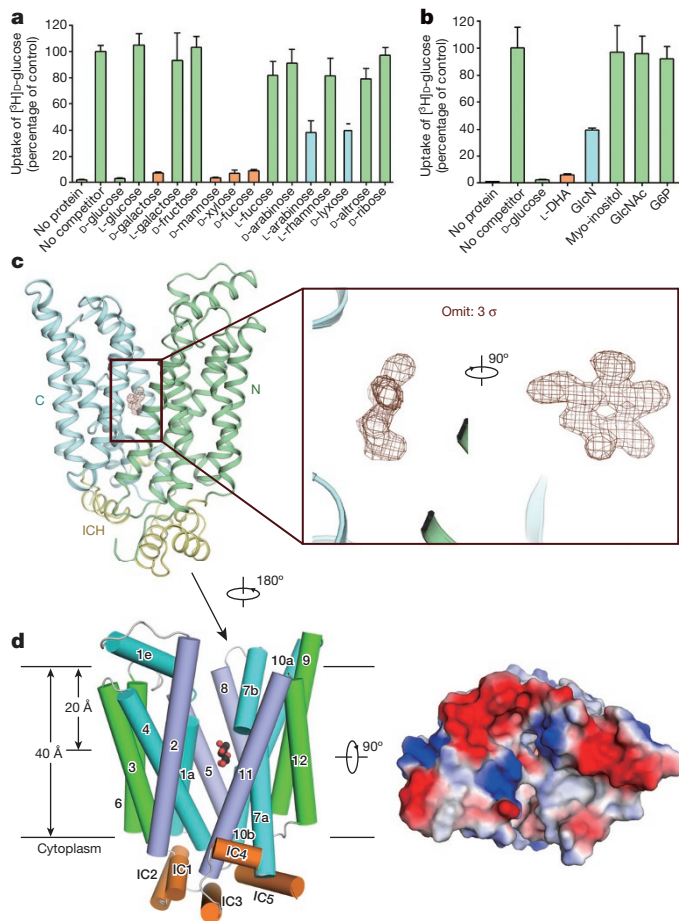


Figure 1 | Structure of human GLUT3(N43T) bound to D-glucose.

a, b, Substrate specificity of GLUT3. The transport of D-[2-³H]glucose by recombinant GLUT3(N43T) protein was examined in proteoliposome-based counterflow assays in the presence of the indicated monosaccharides (**a**) and chemicals (**b**). All the experiments were independently repeated at least three times. Error bars represent s.d. L-DHA, L-dehydroascorbic acid; GlcN, glucosamine; GlcNAc, N-acetylglucosamine; G6P, glucose-6-phosphate. **c**, Overall structure of GLUT3 in the presence of D-glucose. GLUT3 is domain-coloured with pale green, pale cyan and pale yellow for the N-terminal, C-terminal and ICH domains, respectively. The 'omit' electron density of the bound ligand, shown as brown mesh, is contoured at 3 σ . **d**, The structure of glucose-bound GLUT3 exhibits an outward-occluded conformation. The corresponding TMs in the four 3-TM repeats are coloured the same. The ligand is shown as black spheres. The surface electrostatic potential was calculated with PyMol⁴⁹. All structure figures were prepared with PyMol.

may be crucial for specific recognition by GLUT3. Supporting this notion, D-ribose, the C3 epimer of D-xylose, showed no inhibitory effect on the uptake of glucose (Fig. 1a and Extended Data Fig. 1a).

Among the chemicals tested, L-dehydroascorbic acid, which was suggested to be a substrate for GLUTs^{38,39}, effectively inhibited the counterflow of D-glucose by GLUT3. Addition of glucosamine, a reported substrate of GLUT2 (ref. 40), blocked up to 60% of the activity. In contrast, myo-inositol, N-acetylglucosamine or glucose-6-phosphate showed nearly no inhibition (Fig. 1b and Extended Data Fig. 1b). These results, consistent with characterizations performed in distinct systems⁴¹, verified the activity and selectivity of the glycosylation-site-eliminated recombinant GLUT3 protein.

Structure of GLUT3 in complex with D-glucose

The crystals of GLUT3 in the presence of D-glucose were obtained in the P2₁ space group using the lipidic cubic phase (LCP) method. The structure was solved with molecular replacement and refined to 1.5 Å

resolution (Fig. 1c, Extended Data Fig. 2a–d and Extended Data Table 1). The transmembrane region of GLUT3 exhibits a canonical major facilitator superfamily (MFS) fold with the 12 transmembrane segments (TMs) folded into the N-terminal and C-terminal domains, each comprising '3+3' inverted repeats⁴². TM7 and TM10 are discontinuous helices, hence named TM7a/7b and TM10a/10b, respectively (Fig. 1d). The N-terminal and C-terminal domains are connected by four helices (IC1–4), which together with the C-terminal helix IC5 constitute the intracellular helical (ICH) domain.

After assignment and refinement of the polypeptide chain of GLUT3 (residues 1–470), the omit electron density for a bound D-glucose was unambiguously recognized in the central cavity (Fig. 1c). The ligand is occluded from either side of the membrane in the outward-facing GLUT3. Therefore, the structure represents a substrate-bound and outward-occluded state (Fig. 1d). In addition to D-glucose, three monoolein molecules, which were the major components of LCP, were identified (Extended Data Fig. 2e, f).

Recognition of α - and β -anomers of D-glucose by GLUT3

Extensive inter-domain interactions constitute the extracellular and intracellular gates as well as the side walls that insulate the bound ligand from the surrounding environment (Extended Data Fig. 3 and Supplementary Discussion). The high resolution provides unprecedented clarity towards substrate recognition by GLUTs. It is of particular interest that the 2F_o – F_c electron density revealed the existence of both α - and β -D-glucose anomers. Despite the prevailing presence of β -D-glucose in aqueous solution, the α -anomer exhibits a dominant occupancy of approximately 69% in the refined structure (Fig. 2a, b).

D-glucose is bound asymmetrically within the central cavity (Fig. 2c, d and Extended Data Fig. 4a). Located halfway across the membrane height, it stands closer to the C-terminal domain, which provides the primary substrate accommodation site in the centre of its transport-path-facing surface. Six polar residues from the C-terminal domain, including Gln280 and Gln281 on TM7a, Asn286 on TM7b, Asn315 on TM8, Glu378 on TM10a, and Trp386 on TM10b, contribute eight hydrogen bonds to coordinate D-glucose. With respect to the N-terminal domain, D-glucose is closer to TM1 and TM5. Gln159 on TM5 is the only polar residue from the N-terminal domain that engages in hydrogen bonding to D-glucose (Fig. 2d–f).

The α - and β -D-glucose anomers are similarly coordinated by GLUT3 except for the variation at C1-OH (Fig. 2e, f). The α - and β -C1-OH are recognized by Trp386 and Gln280, respectively. The ring oxygen and C1-OH in both anomers are hydrogen bonded to the side group of Gln159. The C2, C3 and C6 hydroxyls are each coordinated by two hydrogen bonds, including those between C6-OH and Asn315 and Glu378, C2-OH and Gln280 and Trp386, and C3-OH and Gln281 and Asn286. The C4-OH forms a single hydrogen bond with Asn286 (Fig. 2e, f). In addition to the polar interactions, the carbon backbone of the sugar ring is surrounded by hydrophobic residues including Phe24 on TM1, Ile162 and Ile166 on TM5, Ile285 and Phe289 on TM7b, and Phe377 on TM10b (Fig. 2g). A monoolein molecule was found to participate in hydrogen bonding with D-glucose. Although the monoolein molecule should be physiologically irrelevant, similar indirect hydrogen bonds between glucose and polar residues may be mediated through water molecules under physiological conditions (Extended Data Fig. 4b).

Structures of GLUT3 bound to maltose

While working with crystallization of glucose-bound GLUT3, we attempted to capture the outward-open state of GLUTs by exploiting exofacial competitors^{43,44}. Details of this work can be found in the Supplementary Discussion and Extended Data Fig. 5. The structures of GLUT3 in complex with maltose were captured in two conformations, outward-open at 2.6 Å and outward-occluded at 2.4 Å resolutions, respectively (Fig. 3, Extended Data Fig. 6 and Extended Data

Figure 2 | Coordination of the α - and β -D-glucose anomers by GLUT3. **a, b**, Both α - and β -anomers of D-glucose are identified in the structure of GLUT3. The $2F_o - F_c$ electron density maps, shown as blue mesh, for α - and β -D-glucose are contoured at 2σ and 1σ , respectively. **c**, The bound glucose is predominantly coordinated by the C-terminal domain. A cut-open side view of the semi-transparent surface electrostatic potential is shown. **d**, The position of the bound glucose with respect to the C-terminal and N-terminal domains. The substrate-facing sides of the C-terminal and N-terminal domains are shown in surface and cartoon representations. Only the α -anomer is shown. **e, f**, Coordination of α - and β -D-glucose by GLUT3 through polar interactions. The α - (**e**) and β - (**f**) anomers are coloured black and silver, respectively. Hydrogen bonds are represented by red dashed lines. **g**, Coordination of glucose by GLUT3 through van der Waals interactions. The residues from the N-terminal and C-terminal domains are coloured green and cyan, respectively.

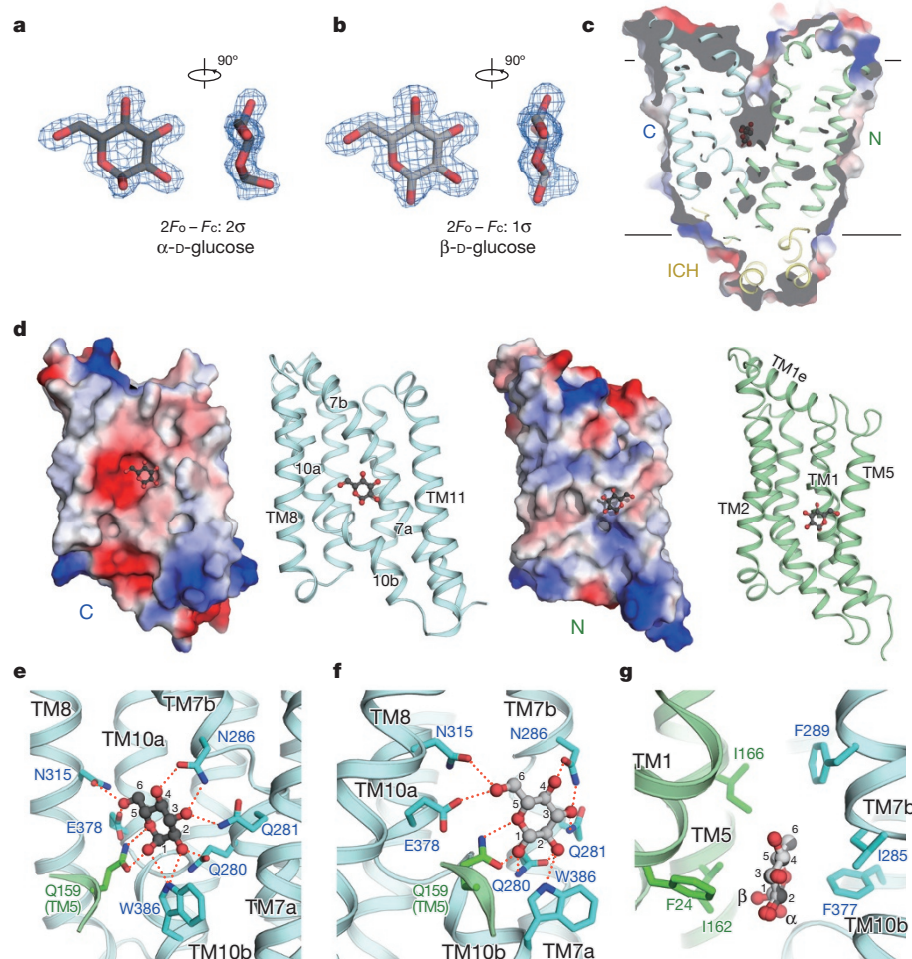


Table 2). Please refer to the Supplementary Discussion and Extended Data Fig. 7 for detailed analysis of maltose coordination in the two conformations. Briefly, the maltose-bound, outward-occluded structure is virtually indistinguishable from the glucose-bound GLUT3 with an overall root mean square deviation of 0.25 Å. The second glucose unit (Glc2) of maltose completely overlaps with D-glucose when the two structures are superimposed. The coordination of Glc2 is nearly identical to that of glucose except for Asn286, whose side group exhibits a distinct rotamer that recognizes the C3-OH of Glc1 (Extended Data Fig. 7a, b).

Comparison of the outward-open and -occluded states

Subtle relative rotation of the N-terminal and C-terminal domains towards the central cavity on the extracellular side is observed during the state transition from outward-open to outward-occluded. The N-terminal domains remain nearly rigid in the two structures, whereas prominent local rearrangements occur to TM7b in the C-terminal domain (Fig. 4a, b and Supplementary Video 1).

To achieve the conformational switch from outward-open to outward-occluded, TM7b, which consists of four helical turns, is partly unwound and bent in the middle such that the first two helical turns tilt inwards. Meanwhile these two helical turns undergo an axial rotation by approximately 60 degrees, leading to the relocation of the bulky residue Tyr290 and the substrate-coordinating residue Asn286 into the transport path (Fig. 4b). Notably, an invariant glycine (Gly284 in GLUT3) constitutes the kink preceding TM7b, which may provide the flexibility for the pronounced structural shift (Supplementary Fig. 1). Whereas the endofacial region of the TM domain remains nearly unchanged (Fig. 4a, right panel), the ICH domain exhibits minor intra-domain rearrangements with the inward

motion of helices IC1/2/3/5 by 1 to 2 Å during the outward-open to outward-occluded transition (Fig. 4c).

Alternating access

GLUT3 shares sequence identity of 66% and similarity of 80% with GLUT1 (Supplementary Fig. 1). Structural resolution of the two closely related GLUTs in three distinct conformations reveals the molecular basis for the alternating access cycle. The N-terminal domain remains almost rigid during a relative rotation of the two domains, while the discontinuous helices TM7/10 and their adjoining segments in the C-terminal domain undergo prominent local

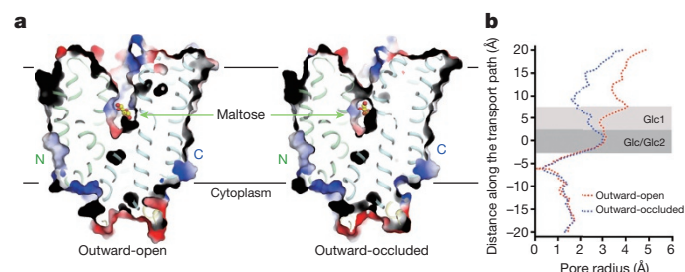


Figure 3 | Structures of maltose-bound GLUT3 in the outward-open and outward-occluded conformations. **a**, Structures of GLUT3 in complex with maltose in the outward-open and outward-occluded states. The cut-open views of the surface electrostatic potential are shown to compare the contours of the central cavities in the two structures. **b**, The van der Waals surface of the two GLUT3 structures was calculated with the program HOLE⁵⁰. The radii of the potential transport path are tabulated. The glucose and maltose binding zones are indicated by grey shades. Glc, glucose.

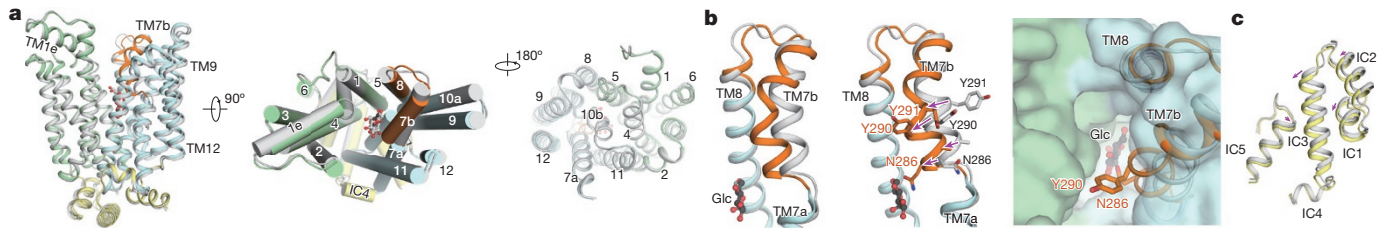


Figure 4 | Conformational changes between the outward-open and outward-occluded GLUT3. **a**, Structural comparison of GLUT3 in two conformations. The outward-occluded GLUT3 is domain-coloured and the outward-open one is coloured silver. The structures are superimposed relative to their N-terminal domains. TM7b and the adjoining segment of TM8 are coloured orange in the outward-occluded structure. The ICH domain is omitted in the right panel, where an intracellular view of the transmembrane domain is shown. Note that the structures of the outward-occluded GLUT3 bound to maltose and glucose are nearly identical (Extended Data Fig. 7b). We hereby use the glucose-bound structure for comparison. **b**, Conformational

rearrangements. TM7b is gradually bent towards the central cavity, while TM10b swings away from the transport path during the outward to inward transition (Fig. 5a–c).

The rigidity of the N-terminal domain and the adaptability of the C-terminal domain may be determined by their distinct structural features (Extended Data Fig. 8). The internal core of the N-terminal domain is relatively hydrophilic. Seven water molecules were identified within the N-terminal domain of the GLUT3 structures. A continuous strip of hydrogen bonds connecting the water

changes of TM7b result in the transition from outward-open to outward-occluded. Right panel, an extracellular view of the GLUT3 structures superimposed against the N-terminal domain. The outward-open GLUT3 is shown in semi-transparent surface representation and TMs 7 and 8 in the two structures are shown as ribbon cartoon. See Supplementary Video 1 for the morph illustrating the conformational changes between the two states. **c**, Conformational shifts of the ICH domain. When the two structures are overlaid relative to the N-terminal domain, the ICH helices exhibit minor intra-domain motions indicated by the purple arrows.

molecules and the polar residues on TM1 and TM4 extends throughout the internal core of the N-terminal domain, likely supporting the rigidity of the N-terminal domain during conformational shift. In contrast, the C-terminal domain is highly hydrophobic. This ‘greasy’ interior may enable the structural adaptability of the C-terminal domain.

Consistent with the extensive polar interactions with the C-terminal domains, the bound D-glucose in the outward-facing GLUT3 and the glucoside of n-nonyl-β-D-glucopyranoside (β-NG)

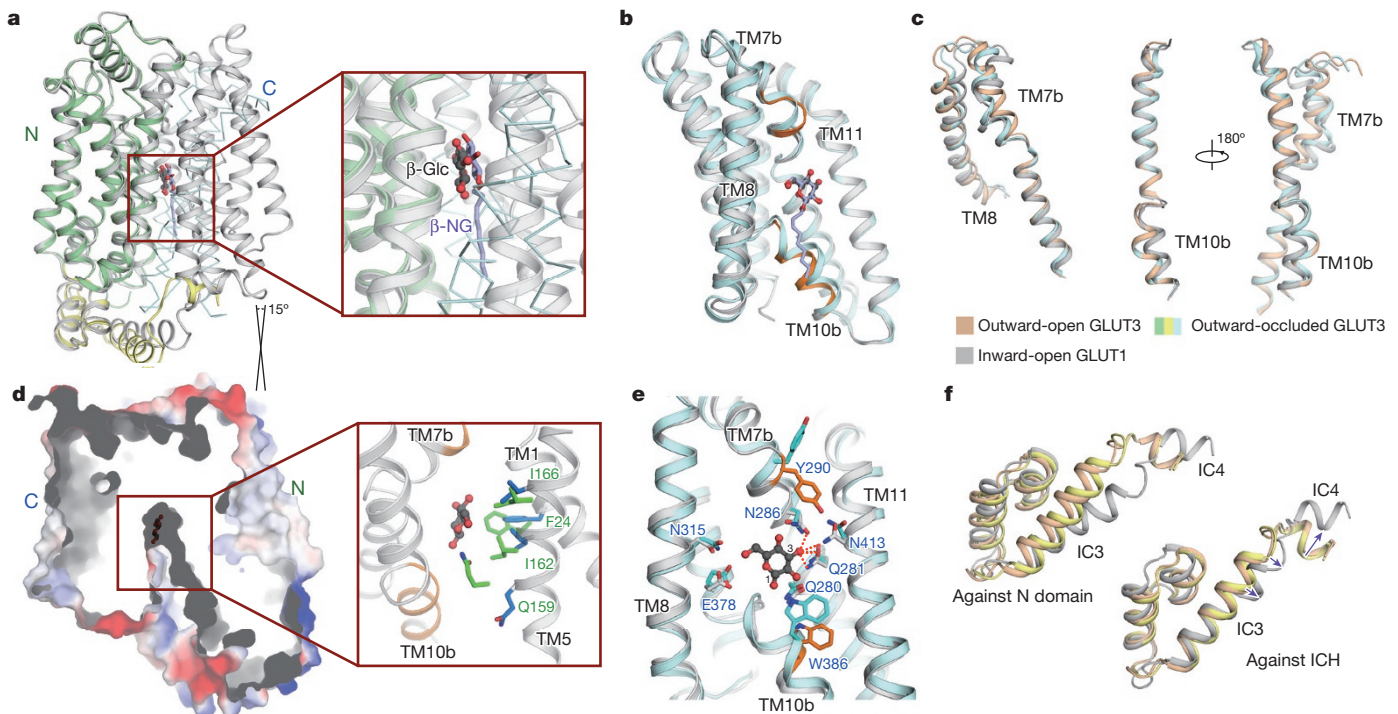


Figure 5 | Alternating access of the glucose-binding site in GLUTs.

a, Structural comparison of glucose-bound GLUT3 with the inward-open GLUT1. The two structures are superimposed relative to their N-terminal domains. GLUT3 is domain-coloured and GLUT1 (PDB accession code: 4PYP) is coloured silver. Inset, when the N-terminal domains of the two structures are superimposed, the bound ligands are not overlapped. For visual simplicity, the C-terminal domain of GLUT3 is shown as a thin ribbon. **b**, Intra-domain rearrangements of the C-terminal domains between the inward-open GLUT1 and outward-occluded GLUT3. The segments that exhibit local structural shifts are coloured orange in GLUT1. The structures of GLUT3 and GLUT1 are superimposed relative to their C-terminal domains in panels **b**–**e**. See Supplementary Video 2 for the morph that illustrates the conformational changes. **c**, TM7b and TM10b undergo prominent conformational changes in

the three indicated structures. **d**, Modelled glucose-binding in the inward-open GLUT1. The cut-open view of the semi-transparent surface electrostatic potential of GLUT1 is shown. Inset, the N-terminal domain residues may no longer engage in glucose-coordination in the inward-open conformation. The N-terminal domain residues that contribute to glucose binding in the outward-facing GLUT3 are shown as green sticks; the corresponding residues in the inward-open GLUT1 are coloured blue. All the residues are numbered as in GLUT3. **e**, Rearrangements of glucose-coordination between the outward-occluded GLUT3 and inward-open GLUT1. The C-domain ligand-binding residues that exhibit prominent changes between the two states are coloured orange in the inward-open conformation. **f**, Conformational changes of the ICH domain. The colour code of the three structures follows that in panel **c**.

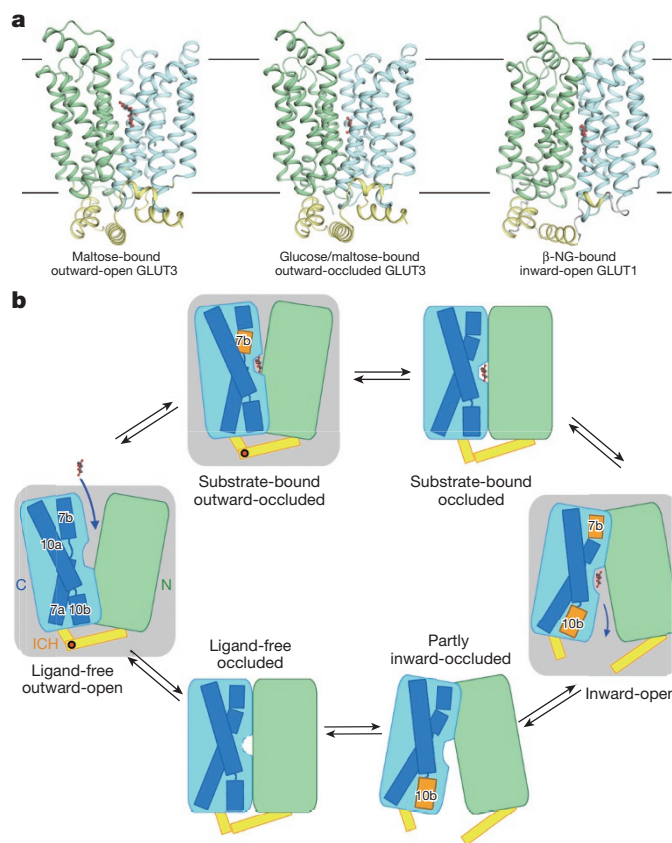


Figure 6 | Updated working model of GLUTs. **a**, An overview of the resolved structures of human GLUT1 and GLUT3. See Supplementary Video 3 for the morph that illustrates the conformational changes between the three structures. **b**, Schematic illustration of the alternating access cycle of GLUTs. The rearrangements of the substrate-binding site and the local structural shifts of TM7b and TM10b during the transport cycle are highlighted. The shaded states refer to the structures shown in panel **a**. The N-terminal, C-terminal and ICH domains are coloured green, cyan and yellow, respectively. The structural elements that undergo prominent local shifts during state transition are highlighted in orange.

in the inward-facing GLUT1 completely overlap when the C-terminal domains, but not N-terminal domains, are superimposed (Fig. 5a, b). We modelled β -D-glucose in the structure of inward-open GLUT1 at the position of the glucoside of β -NG (Fig. 5d). As all the concerned residues are invariant between GLUT1 and GLUT3, we used the residue numbering of GLUT3.

In the inward-open structure, the N-terminal domain residues no longer engage in ligand binding (Fig. 5d, inset). Within the C-terminal domain, local structural shifts result in rearrangement of the substrate-binding site (Fig. 5e). Trp386 loses contact with the ligand due to the outward swing of TM10b. Consequently, the ring oxygen and α -C1-OH may lose interactions with the protein in this conformation (Supplementary Video 2).

In addition to the local shift of TM7/TM10, the ICH domain also undergoes pronounced conformational changes. Because of the preferential association of helices IC1/2 with the N-terminal domain and IC4 with the C-terminal domain, the intervening helix IC3 may function like a 'door closer' that restrains the opening degree of the N-terminal and C-terminal domains on the intracellular side (Fig. 5f and Supplementary Video 3). Helix IC5 is missing in the structure of GLUT1, implying its intrinsic flexibility due to the potential loss of interactions with other ICH helices in the inward-open state³² (Extended Data Fig. 3c). The structural observation supports the notion that the ICH domain may serve as a latch to stabilize the outward-facing conformation of GLUTs^{32,33}.

Discussion

The structural analyses of GLUTs presented here and previously (Fig. 6a) provide the molecular basis to address the long-standing questions on substrate recognition and transport by GLUTs. The discrimination of α - and β -D-glucose by GLUTs and whether anomericization is required has been controversial for decades^{45–47}. The 1.5 Å structure of glucose-bound GLUT3 reveals that GLUTs can recognize both anomers, hence anomericization may not be required for D-glucose transport by GLUTs (Fig. 2e, f).

The structures also provide interpretation for the 'asymmetry' of ligand binding from the endo- and exofacial sides of GLUTs⁴⁸ (Figs 2, 5 and 6b). The C-terminal domain provides the primary yet partial substrate-binding site composed of polar residues including Gln280 and Gln281 on TM7b, Asn315 on TM8, and Glu378 on TM10a. Arrival of the substrate at the primary site from either the exo- or endofacial side may induce conformational changes including the local shifts of TM7b and TM10b along with the relative rotation of the N-terminal and C-terminal domains. Therefore, the substrate-binding site may undergo dynamic rearrangements during a transport cycle (Fig. 6b and Supplementary Video 2).

The advances in the structural elucidation of GLUT3 and GLUT1 provide the framework for understanding a wealth of experimental data of GLUTs over the last half century and provide the foundation for further kinetic and thermodynamic studies of this important class of transporters. The high-resolution structures offer important insight into substrate selectivity, which may illuminate the rational design and optimization of ligands targeting the Warburg effect through GLUTs.

Online Content Methods, along with any additional Extended Data display items and Source Data, are available in the online version of the paper; references unique to these sections appear only in the online paper.

Received 6 January; accepted 12 June 2015.

Published online 15 July 2015.

- Nelson, D. L. & Cox, M. M. *Lehninger Principles of Biochemistry* (W. H. Freeman, 2008).
- Hediger, M. A., Clemençon, B., Burrier, R. E. & Bruford, E. A. The ABCs of membrane transporters in health and disease (SLC series): introduction. *Mol. Aspects Med.* **34**, 95–107 (2013).
- Mueckler, M. & Thorens, B. The SLC2 (GLUT) family of membrane transporters. *Mol. Aspects Med.* **34**, 121–138 (2013).
- Manolescu, A. R., Witkowska, K., Kinnaird, A., Cessford, T. & Cheeseman, C. Facilitated hexose transporters: new perspectives on form and function. *Physiology* **22**, 234–240 (2007).
- LeFevre, P. G. Evidence of active transfer of certain non-electrolytes across the human red cell membrane. *J. Gen. Physiol.* **31**, 505–527 (1948).
- Kasahara, M. & Hinkle, P. C. Reconstitution and purification of the D-glucose transporter from human erythrocytes. *J. Biol. Chem.* **252**, 7384–7390 (1977).
- Mueckler, M. *et al.* Sequence and structure of a human glucose transporter. *Science* **229**, 941–945 (1985).
- Thorens, B. & Mueckler, M. Glucose transporters in the 21st century. *Am. J. Physiol. Endocrinol. Metab.* **298**, E141–E145 (2010).
- Dick, A. P., Harik, S. I., Klip, A. & Walker, D. M. Identification and characterization of the glucose transporter of the blood-brain barrier by cytochalasin B binding and immunological reactivity. *Proc. Natl Acad. Sci. USA* **81**, 7233–7237 (1984).
- Maher, F., Vannucci, S. J. & Simpson, I. A. Glucose transporter proteins in brain. *FASEB J.* **8**, 1003–1011 (1994).
- Thorens, B., Sarkar, H. K., Kaback, H. R. & Lodish, H. F. Cloning and functional expression in bacteria of a novel glucose transporter present in liver, intestine, kidney, and β -pancreatic islet cells. *Cell* **55**, 281–290 (1988).
- Fukumoto, H. *et al.* Sequence, tissue distribution, and chromosomal localization of mRNA encoding a human glucose transporter-like protein. *Proc. Natl Acad. Sci. USA* **85**, 5434–5438 (1988).
- Simpson, I. A. *et al.* The facilitative glucose transporter GLUT3: 20 years of distinction. *Am. J. Physiol. Endocrinol. Metab.* **295**, E242–E253 (2008).
- James, D. E., Brown, R., Navarro, J. & Pilch, P. F. Insulin-regulatable tissues express a unique insulin-sensitive glucose transport protein. *Nature* **333**, 183–185 (1988).
- Birnbaum, M. J. Identification of a novel gene encoding an insulin-responsive glucose transporter protein. *Cell* **57**, 305–315 (1989).
- Mueckler, M. Facilitative glucose transporters. *Eur. J. Biochem.* **219**, 713–725 (1994).
- Pascual, J. M. *et al.* GLUT1 deficiency and other glucose transporter diseases. *Eur. J. Endocrinol.* **150**, 627–633 (2004).
- Santer, R. *et al.* Mutations in GLUT2, the gene for the liver-type glucose transporter, in patients with Fanconi-Bickel syndrome. *Nature Genet.* **17**, 324–326 (1997).

19. Simpson, I. A., Chundu, K. R., Davies-Hill, T., Honer, W. G. & Davies, P. Decreased concentrations of GLUT1 and GLUT3 glucose transporters in the brains of patients with Alzheimer's disease. *Ann. Neurol.* **35**, 546–551 (1994).
20. Macheda, M. L., Rogers, S. & Best, J. D. Molecular and cellular regulation of glucose transporter (GLUT) proteins in cancer. *J. Cell. Physiol.* **202**, 654–662 (2005).
21. Amann, T. & Hellerbrand, C. GLUT1 as a therapeutic target in hepatocellular carcinoma. *Expert Opin. Ther. Targets* **13**, 1411–1427 (2009).
22. Shim, B. Y. *et al.* Glucose transporter 1 (GLUT1) of anaerobic glycolysis as predictive and prognostic values in neoadjuvant chemoradiotherapy and laparoscopic surgery for locally advanced rectal cancer. *Int. J. Colorectal Dis.* **28**, 375–383 (2013).
23. Ramani, P., Headford, A. & May, M. T. GLUT1 protein expression correlates with unfavourable histologic category and high risk in patients with neuroblastic tumours. *Virchows Arch.* **462**, 203–209 (2013).
24. Flavahan, W. A. *et al.* Brain tumor initiating cells adapt to restricted nutrition through preferential glucose uptake. *Nature Neurosci.* **16**, 1373–1382 (2013).
25. Airley, R. E. & Mobasher, A. Hypoxic regulation of glucose transport, anaerobic metabolism and angiogenesis in cancer: novel pathways and targets for anticancer therapeutics. *Chemotherapy* **53**, 233–256 (2007).
26. Kaira, K. *et al.* Biological significance of ¹⁸F-FDG uptake on PET in patients with non-small-cell lung cancer. *Lung Cancer* **83**, 197–204 (2013).
27. Gallamini, A., Zwarthoed, C. & Borra, A. Positron emission tomography (PET) in oncology. *Cancers* **6**, 1821–1889 (2014).
28. Calvaresi, E. C. & Hergenrother, P. J. Glucose conjugation for the specific targeting and treatment of cancer. *Chem. Sci.* **4**, 2319–2333 (2013).
29. Jardetzky, O. Simple allosteric model for membrane pumps. *Nature* **211**, 969–970 (1966).
30. Shi, Y. Common folds and transport mechanisms of secondary active transporters. *Annu. Rev. Biophys.* **42**, 51–72 (2013).
31. Smirnova, I., Kasho, V. & Kaback, H. R. Lactose permease and the alternating access mechanism. *Biochemistry* **50**, 9684–9693 (2011).
32. Deng, D. *et al.* Crystal structure of the human glucose transporter GLUT1. *Nature* **510**, 121–125 (2014).
33. Sun, L. *et al.* Crystal structure of a bacterial homologue of glucose transporters GLUT1–4. *Nature* **490**, 361–366 (2012).
34. Quistgaard, E. M., Low, C., Moberg, P., Tresaugues, L. & Nordlund, P. Structural basis for substrate transport in the GLUT-homology family of monosaccharide transporters. *Nature Struct. Mol. Biol.* **20**, 766–768 (2013).
35. Wisedchaisri, G., Park, M. S., Iadanza, M. G., Zheng, H. & Gonen, T. Proton-coupled sugar transport in the prototypical major facilitator superfamily protein XylE. *Nature Commun.* **5**, 4521 (2014).
36. Lacko, L., Wittke, B. & Geck, P. The temperature dependence of the exchange transport of glucose in human erythrocytes. *J. Cell. Physiol.* **82**, 213–218 (1973).
37. Chen, C. C. *et al.* Human erythrocyte glucose transporter: normal asymmetric orientation and function in liposomes. *Proc. Natl Acad. Sci. USA* **83**, 2652–2656 (1986).
38. Rumsey, S. C. *et al.* Glucose transporter isoforms GLUT1 and GLUT3 transport dehydroascorbic acid. *J. Biol. Chem.* **272**, 18982–18989 (1997).
39. Rumsey, S. C. *et al.* Dehydroascorbic acid transport by GLUT4 in *Xenopus* oocytes and isolated rat adipocytes. *J. Biol. Chem.* **275**, 28246–28253 (2000).
40. Uldry, M., Ibberson, M., Hosokawa, M. & Thorens, B. GLUT2 is a high affinity glucosamine transporter. *FEBS Lett.* **524**, 199–203 (2002).
41. Maher, F., Davies-Hill, T. M. & Simpson, I. A. Substrate specificity and kinetic parameters of GLUT3 in rat cerebellar granule neurons. *Biochem. J.* **315**, 827–831 (1996).
42. Yan, N. Structural advances for the major facilitator superfamily (MFS) transporters. *Trends Biochem. Sci.* **38**, 151–159 (2013).
43. Carruthers, A. & Helgerson, A. L. Inhibitions of sugar transport produced by ligands binding at opposite sides of the membrane. Evidence for simultaneous occupation of the carrier by maltose and cytochalasin B. *Biochemistry* **30**, 3907–3915 (1991).
44. Colville, C. A., Seatter, M. J., Jess, T. J., Gould, G. W. & Thomas, H. M. Kinetic analysis of the liver-type (GLUT2) and brain-type (GLUT3) glucose transporters in *Xenopus* oocytes: substrate specificities and effects of transport inhibitors. *Biochem. J.* **290**, 701–706 (1993).
45. Janoshazi, A. & Solomon, A. K. Initial steps of alpha- and beta-D-glucose binding to intact red cell membrane. *J. Membr. Biol.* **132**, 167–178 (1993).
46. Leitch, J. M. & Carruthers, A. α - and β -monosaccharide transport in human erythrocytes. *Am. J. Physiol. Cell Physiol.* **296**, C151–C161 (2009).
47. Carruthers, A. & Melchior, D. L. Transport of alpha- and beta-D-glucose by the intact human red cell. *Biochemistry* **24**, 4244–4250 (1985).
48. Barnett, J. E., Holman, G. D. & Munday, K. A. An explanation of the asymmetric binding of sugars to the human erythrocyte sugar-transport systems. *Biochem. J.* **135**, 539–541 (1973).
49. DeLano, W. L. The PyMOL molecular graphics system (Schrödinger, 2002).
50. Smart, O. S., Goodfellow, J. M. & Wallace, B. A. The pore dimensions of gramicidin A. *Biophys. J.* **65**, 2455–2460 (1993).

Supplementary Information is available in the online version of the paper.

Acknowledgements We thank the Tsinghua University Branch of China National Center for Protein Sciences (Beijing) for providing the facility support. The computation was completed on the "Explorer 100" cluster system of Tsinghua National Laboratory for Information Science and Technology. This work was supported by funds from the Ministry of Science and Technology of China (2015CB910101, 2011CB910501, 2014ZX09507003006) and National Natural Science Foundation of China (projects 31130002 and 31125009). The research of N. Y. was supported in part by an International Early Career Scientist grant from the Howard Hughes Medical Institute and an endowed professorship from Bayer Healthcare.

Author Contributions N.Y. conceived the project. D.D., P.S. and N.Y. designed all experiments. D.D., P.S., C.Y., X.J., L.X., W.R., K.H., M.Y. and S.F. performed the experiments. D.D., P.S., C.Y., M.K. and N.Y. analysed the data and contributed to manuscript preparation. N.Y. wrote the manuscript.

Author Information The X-ray crystallographic coordinates and structure factor files of the three human GLUT3 structures have been deposited in the Protein Data Bank (PDB) with the accession codes 4ZW9, 4ZWB, and 4ZWC. Reprints and permissions information is available at www.nature.com/reprints. The authors declare no competing financial interests. Readers are welcome to comment on the online version of the paper. Correspondence and requests for materials should be addressed to N.Y. (nyan@tsinghua.edu.cn).

METHODS

Protein purification. The recombinant human glucose transporter GLUT1(N45T) was expressed and purified as described previously³². A similar protocol was applied for the expression and purification of human GLUT3 with minor modifications.

The codon-optimized cDNA of human GLUT3(N43T) was synthesized and subcloned into a modified PfastBac1 vector with an N-terminal 10 × His tag. Following the instructions for the Bac-to-Bac baculovirus expression system (Invitrogen), bacmids were generated in DH10Bac cells. The baculoviruses were generated and amplified in Sf-9 insect cells. For protein expression and purification, the Sf-9 cells were collected 72 h after viral infection, and disrupted using the dounce homogenizer for 80 cycles on ice. The membrane pellets were collected and homogenized in the buffer (25 mM MES pH 6.0 and 150 mM NaCl) containing protease inhibitors (aprotinin at 0.8 μM, pepstatin at 2 μM, and leupeptin at 5 μg ml⁻¹; Amresco), and then solubilized with 2% (w/v) *n*-dodecyl-β-D-maltoside (DDM, Anatrace) at 4 °C for 2 h. The insoluble fraction was precipitated by ultracentrifugation (150,000g) for 30 min at 4 °C. The supernatant was incubated with Ni-NTA resin (Qiagen) for an additional 30 min at 4 °C. The resin was then rinsed with the buffer containing 25 mM MES pH 6.0, 500 mM NaCl, 30 mM imidazole, and 0.06% (w/v) 6-cyclohexyl-1-hexyl-β-D-maltoside (CYMAL-6, Anatrace) three times. The protein was eluted with the washing buffer plus 300 mM imidazole and further concentrated to 10 mg ml⁻¹. For the transport assay, the protein was applied to Superdex 200 10/300 GL (SD200, GE Healthcare) pre-equilibrated with buffer containing 25 mM MES 6.0, 150 mM NaCl, and 0.06% (w/v) CYMAL-6. Peak fractions were collected for the transport assay. For crystallization, 50 mM D-glucose or maltose (Sigma) was added throughout the purification procedure. Concentrated protein was applied to HiTrap Desalting 5 ml (GE Healthcare) in the SD200 buffer plus 50 mM D-glucose or maltose.

Crystallization. GLUT3(N43T), which eluded our extensive crystallization trials using a conventional vapour-diffusion method, was crystallized with the lipid cubic phase (LCP) approach. To prepare the cubic phase for crystallization trials, the protein was concentrated to 30–40 mg ml⁻¹ before mixing with monoolein (Sigma) in 1:1.5 protein to lipid ratio (w/w) using a syringe lipid mixer⁵¹.

For crystallization of glucose-bound GLUT3, the 40 nl meso phase was mixed with 900 nl crystallization buffer for each condition on glass sandwich plates (Shanghai FAlst BioTech) using a robot arm Gryphon (ARI). Crystals appeared within one week with a typical size of 70 μm × 50 μm × 10 μm. These crystals diffracted X-rays to approximately 2.5 Å at SSRF beamline BL17U. Various strategies were exploited to optimize crystals. Finally, the mother liquor containing 28% (v/v) PEG400, 0.1 M HEPES pH 6.8, and 50 mM ammonium citrate gave rise to crystals with a size of approximately 140 μm × 100 μm × 20 μm.

For crystallization trials of maltose-bound GLUT3, 30–45 nl meso phase was overlaid with 800 nl of precipitant solution. Crystals appeared overnight under two similar conditions. The crystals corresponding to the outward-occluded conformation appeared in the crystallization conditions with 38–40% (v/v) PEG 400, 100 mM Mg(CHO₂)₂, 50 mM maltose, and 100 mM ADA pH 6.5. The crystals corresponding to the outward-open conformation appeared in 34% (v/v) PEG 400, 400 mM (NH₄)₂HPO₄, 50 mM maltose and 100 mM ADA pH 6.9. Crystals grew to a maximum size of about 20 × 20 × 5 μm³ at 20 °C within one week.

The crystals were collected using MicroMesh (M3-L18SP-50; MiTeGen) and immediately flash frozen in liquid nitrogen.

Data collection and processing. The data set of glucose-bound GLUT3 was collected at the microfocus beamline BL32XU at SPring-8, Japan. The LCP crystals of GLUT3 were fast-screened with the shutter free strategy developed by SPring-8. Employing the microfocus X-ray beam of size 1 μm × 12 μm and the 'helical collection strategy', we were able to collect a complete data set with a single elongated crystal. All diffraction data sets of maltose bound GLUT3 were also collected at the same beamline. There are generally 10–15 crystals in each MicroMesh. Diffraction data from 7 and 9 crystals in two different lattices were integrated and scaled using HKL2000, respectively⁵². Further processing was carried out with programs from the CCP4 suite⁵³. Data collection and structure refinement statistics are summarized in Extended Data Tables 1 and 2. The data sets were processed with the HKL2000 packages⁵².

Structure determination and refinement. The phase was solved by molecular replacement using PHASER⁵⁴ with GLUT1 (PDB code: 4PYP) as a searching model. The model was first modified by CHAINSAW⁵⁵, then the N-terminal domain and C-terminal domain were taken separately as input ensembles for PHASER. The model was further rebuilt in COOT⁵⁶ and refined with PHENIX⁵⁷. The sequence docking was further aided by sequence alignment with GLUT1. The percentages of occupancy for α- and β-D-glucose were determined by the PHENIX occupancy refinement strategy. The two anomers were considered

as a constrained occupancy group where the occupancies of atoms in α- and β-D-glucose are coupled. The calculated occupancies for the α- and β-anomers were 0.69 and 0.31, respectively. For Supplementary Video 1 the intermediate morphs were obtained with the multiple-chain morphing script^{58,59} for Crystallography & NMR system (CNS)^{60,61}. For Supplementary Video 2, a homology-based structural model of the inward-open GLUT3 was generated based on the structure of GLUT1 using the online SWISS-MODEL workspace^{62–64}.

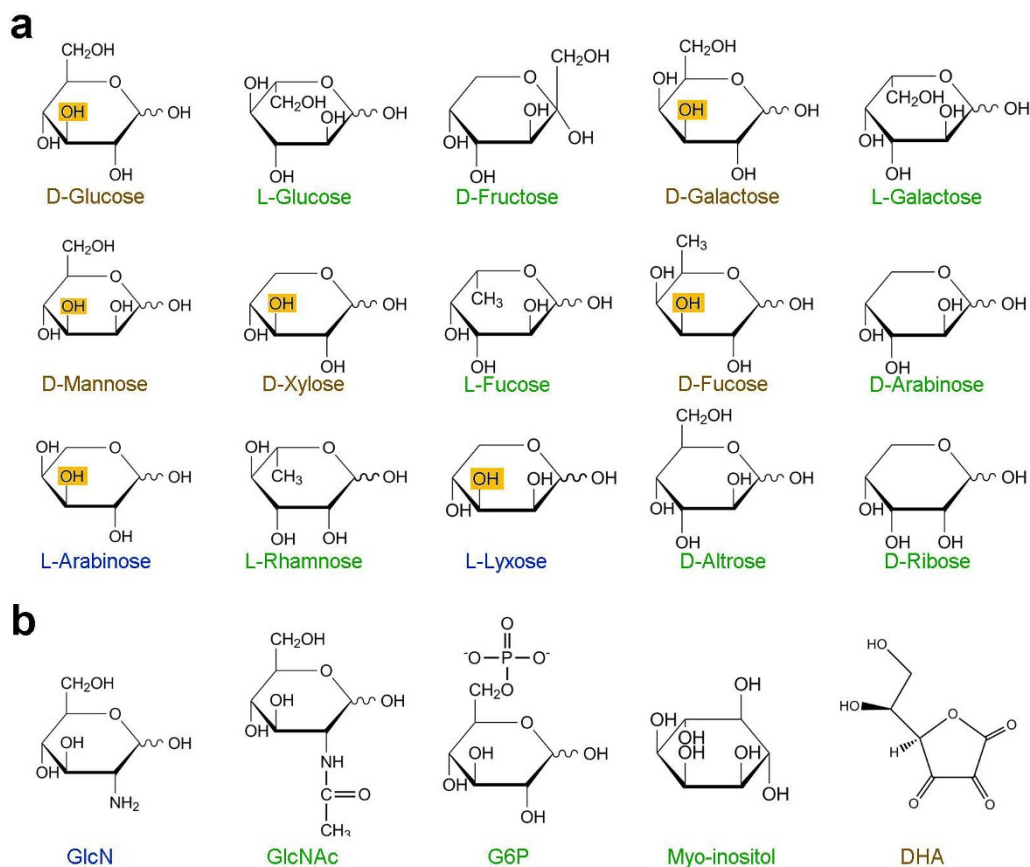
Preparation of liposomes and proteoliposomes. Liposomes were prepared as described previously³³. For the counterflow assay, proteoliposomes were prepared in solution containing KPM 6.5 buffer (50 mM potassium phosphate pH 6.5, 2 mM MgSO₄), 20 mg ml⁻¹ pre-extruded phospholipids (*E. coli* polar lipid extract; Avanti), and 50 mM D-glucose. After incubation with 1% *n*-octyl-β-D-glucopyranoside (β-OG; Anatrace) for 60 min at 4 °C, purified GLUT1(N45T) or GLUT3(N43T) (10 μg protein per mg lipid) was added and incubated for an additional 60 min at 4 °C. β-OG was removed by incubation with 240 mg ml⁻¹ Bio-Beads SM2 (Bio-Rad) overnight and an additional 2 h incubation with 120 mg ml⁻¹ Bio-Beads. Proteoliposomes were then frozen and thawed in liquid nitrogen for five cycles and extruded through membrane filter (PC Membranes 0.4 μm, Avanti). In order to remove the excessive glucose, proteoliposomes were collected by ultracentrifugation at 100,000g for 1 h and washed with ice-cold KPM 6.5 buffer. Finally, the proteoliposomes were resuspended in KPM 6.5 buffer to a final concentration of 100 mg ml⁻¹ (phospholipids).

Counterflow assay. For each assay, 2 μl of concentrated proteoliposomes (GLUT1 or GLUT3) prepared following the above protocol were added into 100 μl KPM 6.5 buffer plus 1 μCi D-[2-³H]glucose (specific radioactivity 21.5 Ci mmol⁻¹, PerkinElmer). The final concentration of the external D-[2-³H]glucose was 0.46 μM. The uptake of radiolabelled substrates was stopped at 30 s by rapidly filtering the solution through 0.22 μm filters (Millipore). The filter membranes were washed with 2 ml ice-cold KPM 6.5 buffer immediately, solubilized with 0.5 ml Optiphase HISAFE 3 (PerkinElmer) and used for liquid scintillation counting with MicroBeta JET (PerkinElmer). Liposomes without protein were tested as a negative control.

For competition assays, the indicated sugars and chemicals were added into the external KPM 6.5 at 50 mM and the transport reaction was stopped at 30 s. The reading of the competition assays was normalized against the one without competitor, which had the uptake of radiolabelled glucose set as 100%. All counter-flow assays were performed at 25 °C and repeated at least three times. Error bars represent s.d.

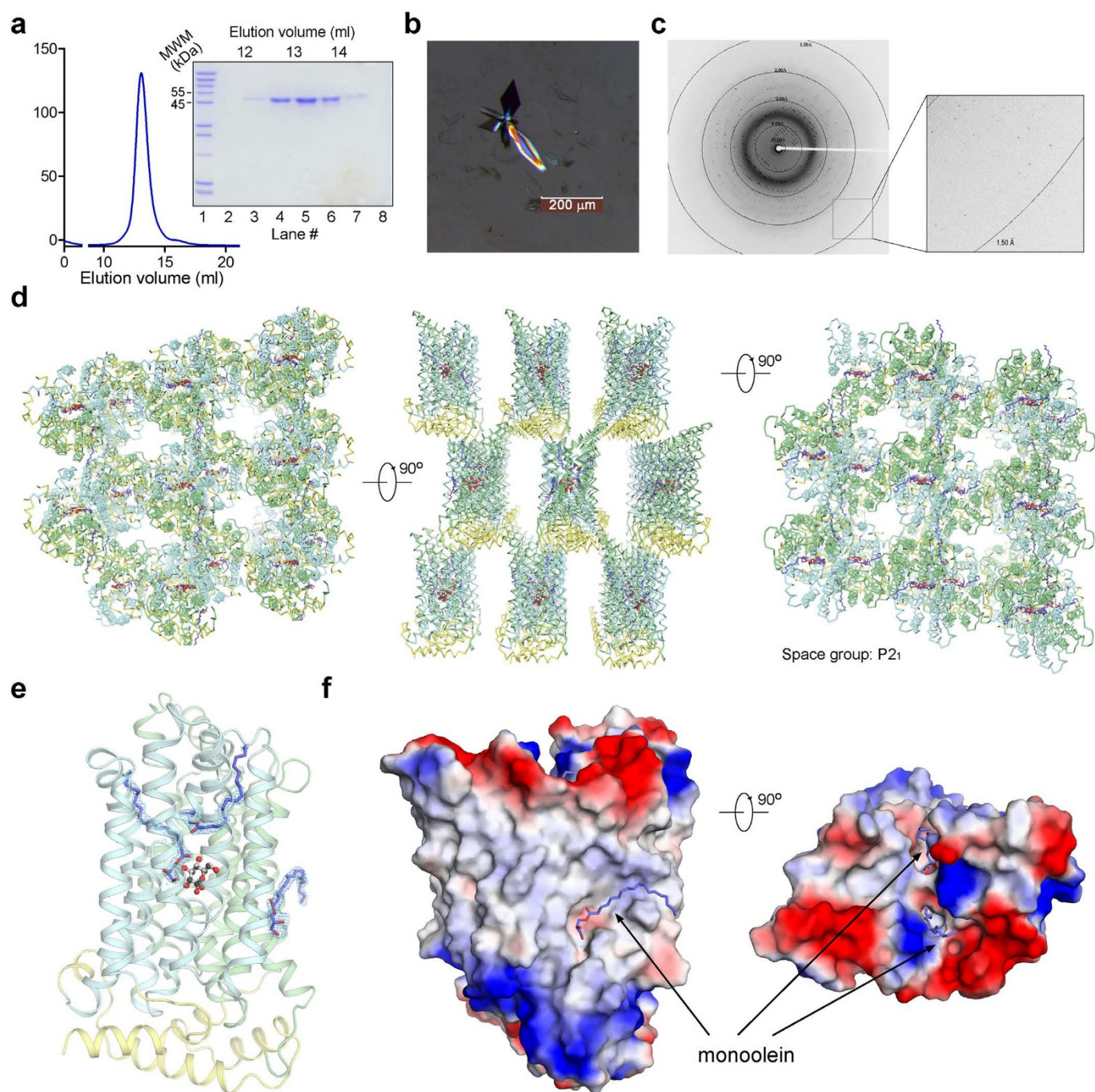
Data reporting. No statistical methods were used to predetermine sample size. The experiments were not randomized. The investigators were not blinded to allocation during experiments and outcome assessment.

- Caffrey, M. & Cherezov, V. Crystallizing membrane proteins using lipidic mesophases. *Nature Protocols* **4**, 706–731 (2009).
- Otwinowski, Z. & Minor, W. Processing of X-ray diffraction data collected in oscillation mode. *Methods Enzymol.* **276**, 307–326 (1997).
- Collaborative Computational Project Number 4. The CCP4 suite: programs for protein crystallography. *Acta Crystallogr. D* **50**, 760–763 (1994).
- McCoy, A. J. *et al.* Phaser crystallographic software. *J. Appl. Crystallogr.* **40**, 658–674 (2007).
- Stein, N. CHAINSAW: a program for mutating pdb files used as templates in molecular replacement. *J. Appl. Crystallogr.* **41**, 641–643 (2008).
- Emsley, P. & Cowtan, K. Coot: model-building tools for molecular graphics. *Acta Crystallogr. D* **60**, 2126–2132 (2004).
- Adams, P. D. *et al.* PHENIX: building new software for automated crystallographic structure determination. *Acta Crystallogr. D Biol. Crystallogr.* **58**, 1948–1954 (2002).
- Echols, N., Milburn, D. & Gerstein, M. MolMovDB: analysis and visualization of conformational change and structural flexibility. *Nucleic Acids Res.* **31**, 478–482 (2003).
- Krebs, W. G. & Gerstein, M. The morph server: a standardized system for analyzing and visualizing macromolecular motions in a database framework. *Nucleic Acids Res.* **28**, 1665–1675 (2000).
- Brünger, A. T. *et al.* Crystallography & NMR system: a new software suite for macromolecular structure determination. *Acta Crystallogr. D* **54**, 905–921 (1998).
- Brünger, A. T. Version 1.2 of the Crystallography and NMR system. *Nature Protocols* **2**, 2728–2733 (2007).
- Arnold, K., Bordoli, L., Kopp, J. & Schwede, T. The SWISS-MODEL workspace: a web-based environment for protein structure homology modelling. *Bioinformatics* **22**, 195–201 (2006).
- Schwede, T., Kopp, J., Guex, N. & Peitsch, M. C. SWISS-MODEL: An automated protein homology-modeling server. *Nucleic Acids Res.* **31**, 3381–3385 (2003).
- Guex, N. & Peitsch, M. C. SWISS-MODEL and the Swiss-PdbViewer: an environment for comparative protein modeling. *Electrophoresis* **18**, 2714–2723 (1997).
- Thompson, J. D., Higgins, D. G. & Gibson, T. J. CLUSTAL W: improving the sensitivity of progressive multiple sequence alignment through sequence weighting, position-specific gap penalties and weight matrix choice. *Nucleic Acids Res.* **22**, 4673–4680 (1994).



Extended Data Figure 1 | Chemical structures of the tested monosaccharides, glucose derivatives, and other chemicals in the competition assay. a, b, The monosaccharides (a) and chemicals (b) that exhibit potent inhibition to the

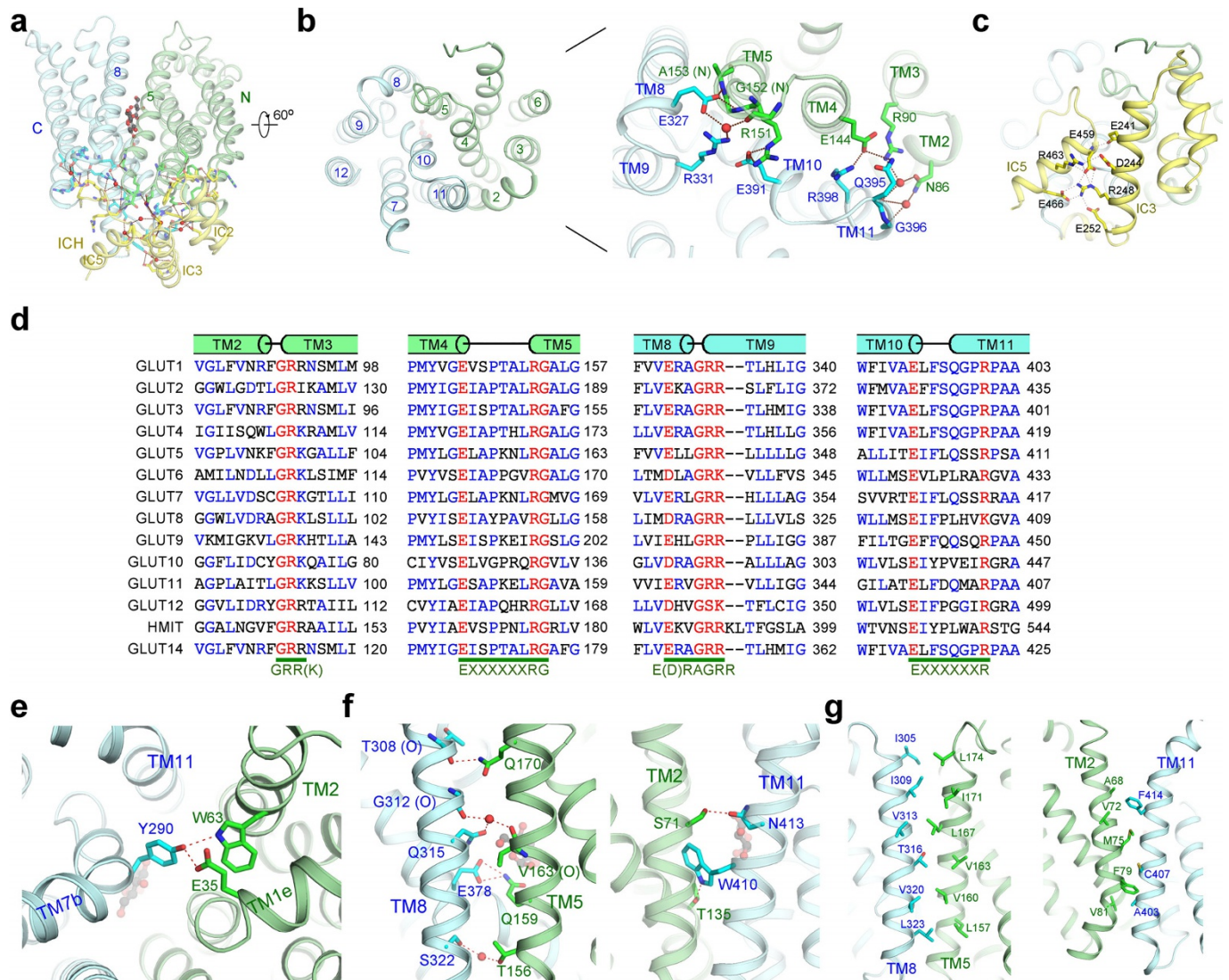
uptake of $[2\text{-}^3\text{H}]\text{glucose}$ in the proteoliposome-based counterflow assay are labelled brown. Those having moderate or no inhibition are labelled blue and green, respectively.



Extended Data Figure 2 | Protein purification, crystallization and structural determination of GLUT3(N43T) in the presence of D-glucose.

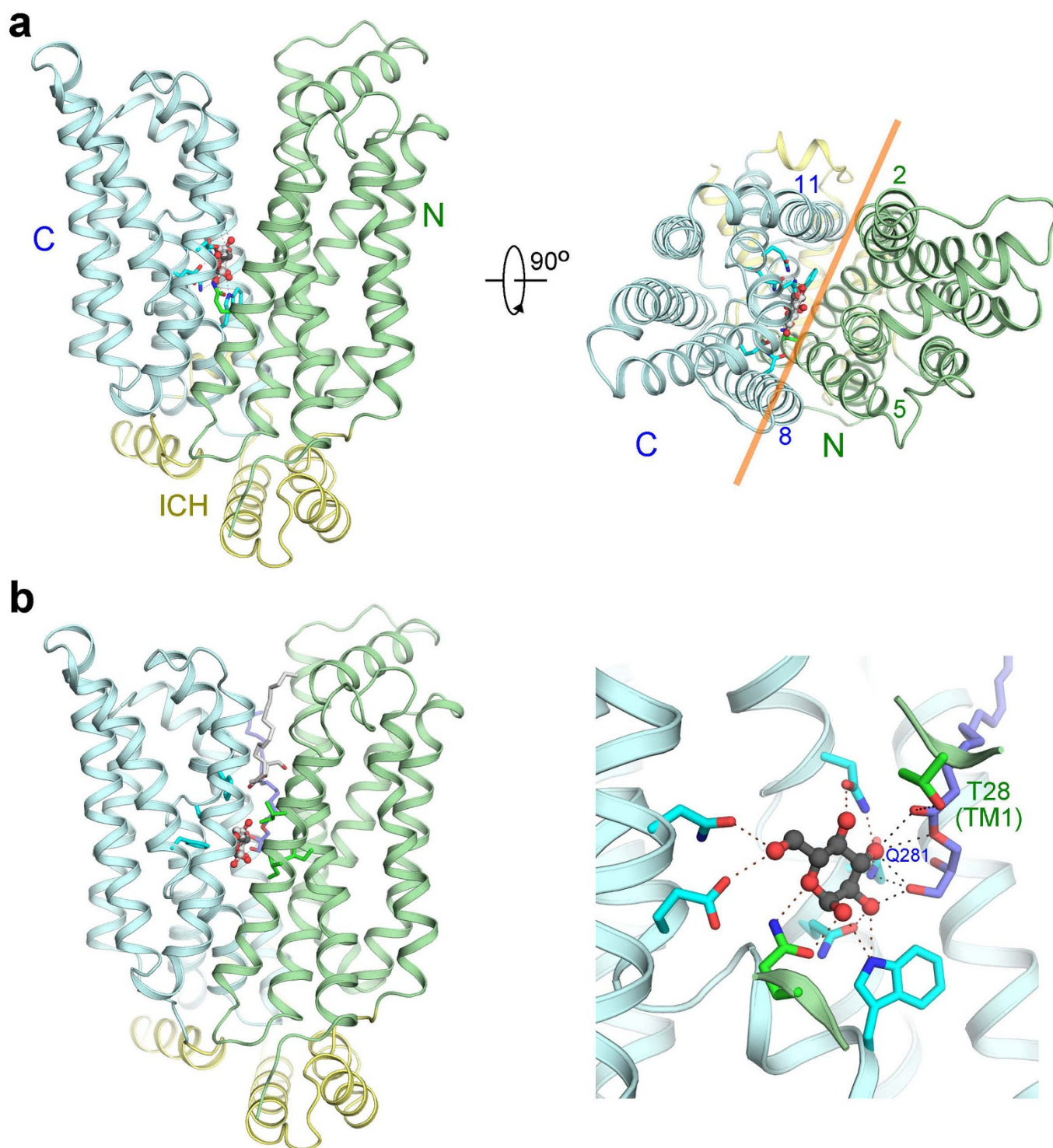
a, A representative chromatogram of the size-exclusion chromatography purification of GLUT3. The peak positions were applied for SDS-PAGE and followed by Coomassie blue staining. **b**, The crystal of GLUT3 used for X-ray diffraction which led to the final structural determination at 1.5 Å resolution. **c**, A representative image of X-ray diffraction. The inset shows the resolution

limit beyond 1.5 Å resolution. **d**, Crystal packing of GLUT3 in the space group of $P2_1$. Three perpendicular views are shown. Each GLUT3 is domain-coloured and shown as a ribbon. The bound glucose is shown as a black sphere and the bound lipid molecules are shown as blue sticks. **e**, Electron densities of three bound monoolein molecules. The $2F_o - F_c$ electron density maps for the bound lipid molecules are contoured at 1.0σ . **f**, Positions of the three bound monoolein molecules relative to the protein structure.



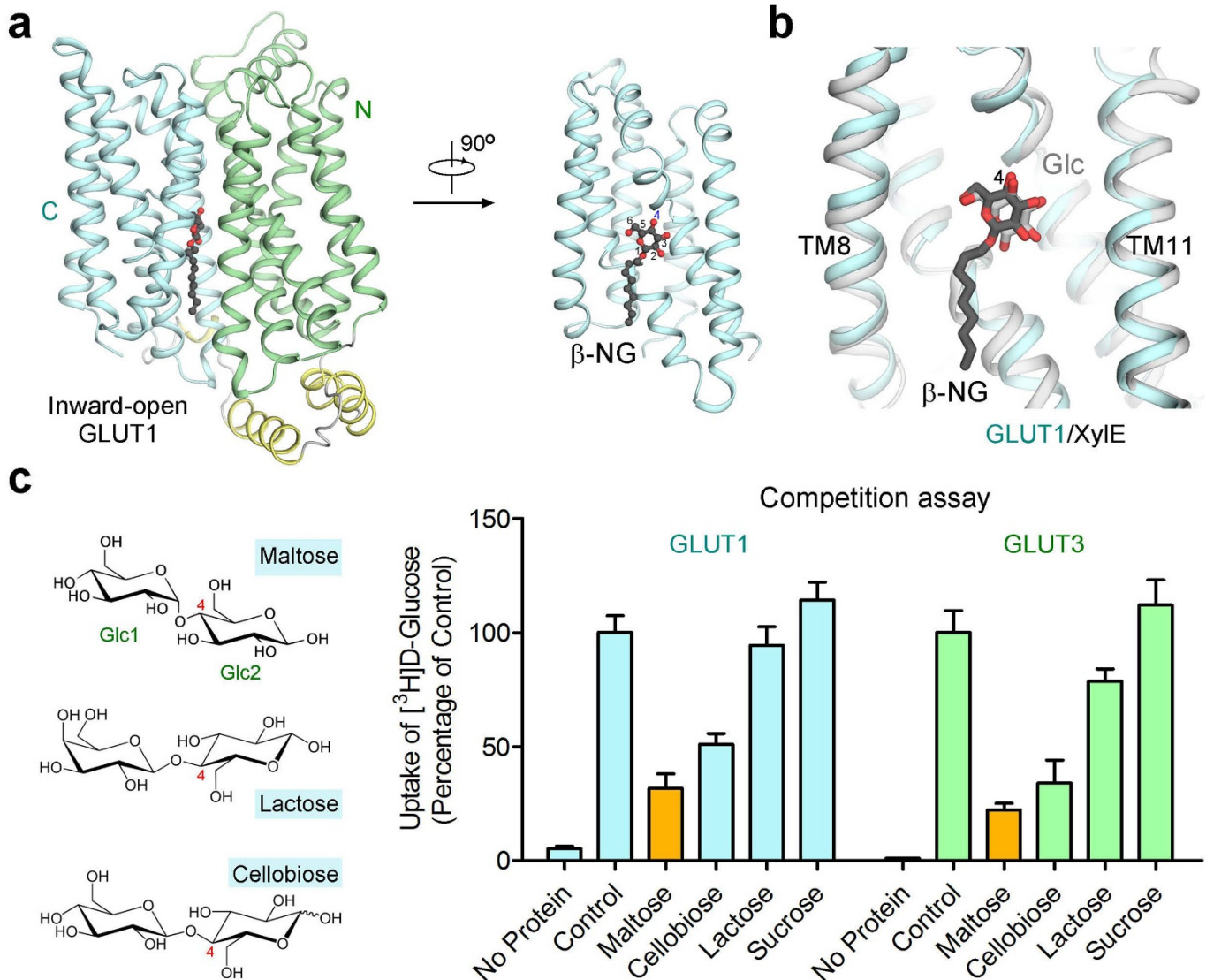
Extended Data Figure 3 | The intracellular and extracellular gates of GLUT3. **a**, The N-terminal, C-terminal and ICH domains interact with each other through an extensive network of direct and water-mediated hydrogen bonds on the intracellular side of the membrane. Water molecules are shown as red spheres. Hydrogen bonds are represented by red dashed lines. **b**, The polar interactions between the N-terminal and C-terminal domains on the intracellular side. An ICH domain-omitted intracellular view is shown. Note the pseudo two-fold symmetry of the overall structure and the interacting residues (inset on the right). These polar interactions partially constitute the intracellular gate of GLUT3 in the outward-facing conformation.

c, Intra-domain interaction of the ICH domain. The polar interactions between helices IC3 and IC5 are shown. **d**, The intracellular gate of GLUT3 involves the Sugar Porter family (SP)-signature motifs. Sequence alignment of the 14 human GLUTs were performed with ClustalW⁶⁵. The secondary structural elements and the SP motifs are shown on the top and bottom, respectively. The residues coloured red are the highly conserved residues that constitute the intracellular gate illustrated in panel **b**. **e**, The extracellular gate of GLUT3 in the outward-occluded state. An extracellular view is shown. **f**, **g**, The polar and hydrophobic residues mediating the lateral interactions of the N-terminal and C-terminal domains.



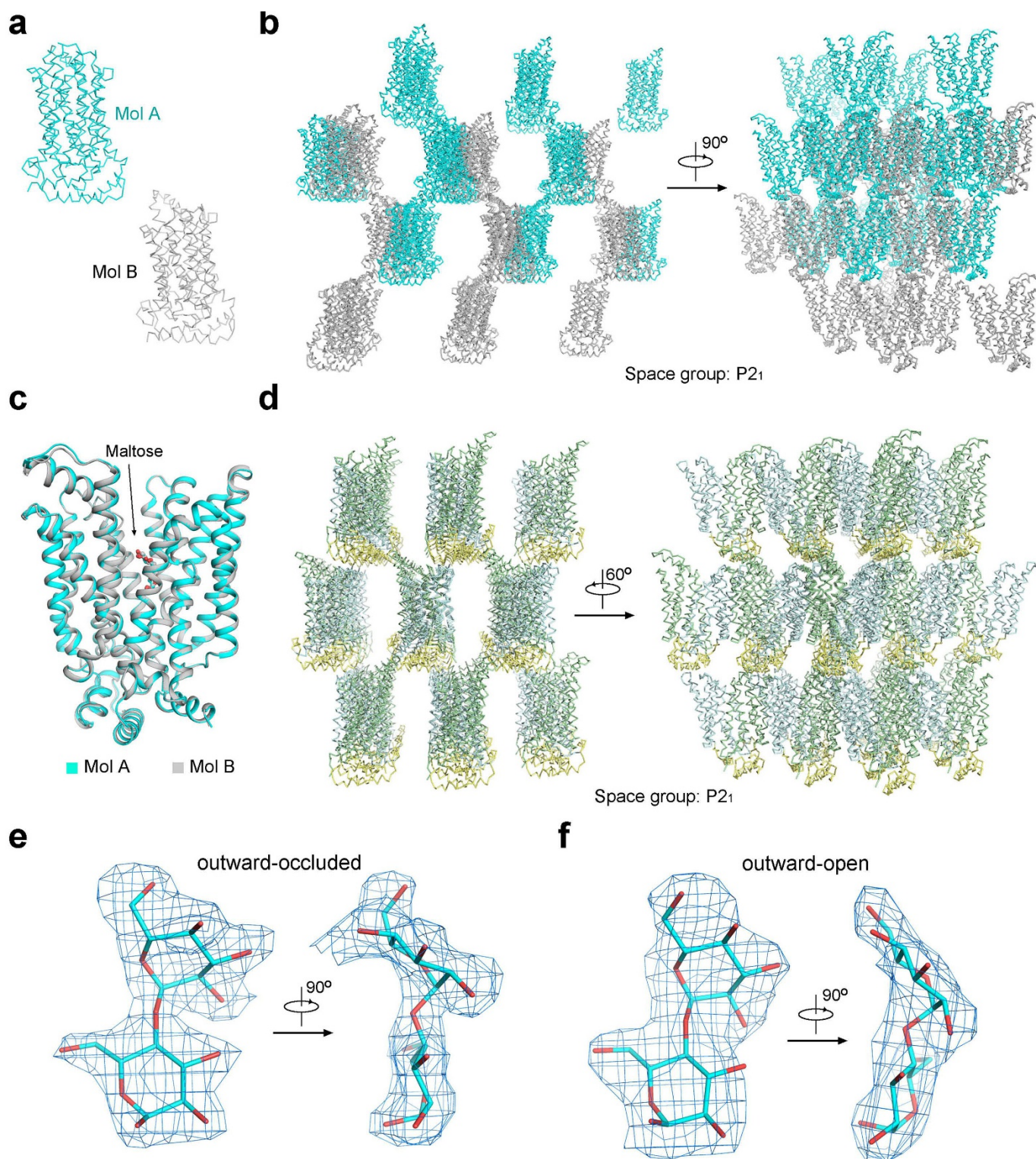
Extended Data Figure 4 | D-glucose coordination by GLUT3. **a**, The C-terminal domain provides the primary accommodation site for glucose in GLUT3. The α - and β -D-glucose anomers are coloured black and silver, respectively. The orange line in the right panel indicates the approximate interface between the N-terminal and C-terminal domains viewed from the extracellular side. Note that the ligand is located closer to the C-terminal

domain. **b**, One monoolein molecule contributes to substrate coordination. The two monoolein molecules bound in the cavity of GLUT3 are coloured silver and light purple. One monoolein molecule mediates indirect hydrogen bonds between C2 and C3 hydroxyl groups of the bound glucose with the side groups of Thr28 and Gln281 of GLUT3. The effect of monoolein on glucose binding and transport has not been characterized.



Extended Data Figure 5 | Attempts to obtain the structure of outward-facing GLUTs. **a**, Presence of the detergent molecule β -NG helped stabilize the inward-open conformation of GLUT1³². **b**, The gluco-pyranoside of β -NG and D-glucose are coordinated similarly by the inward-facing GLUT1 and the outward-facing XylE³³, respectively. In both structures, the C4-OH is positioned towards the extracellular side. **c**, Identification of potential ligands

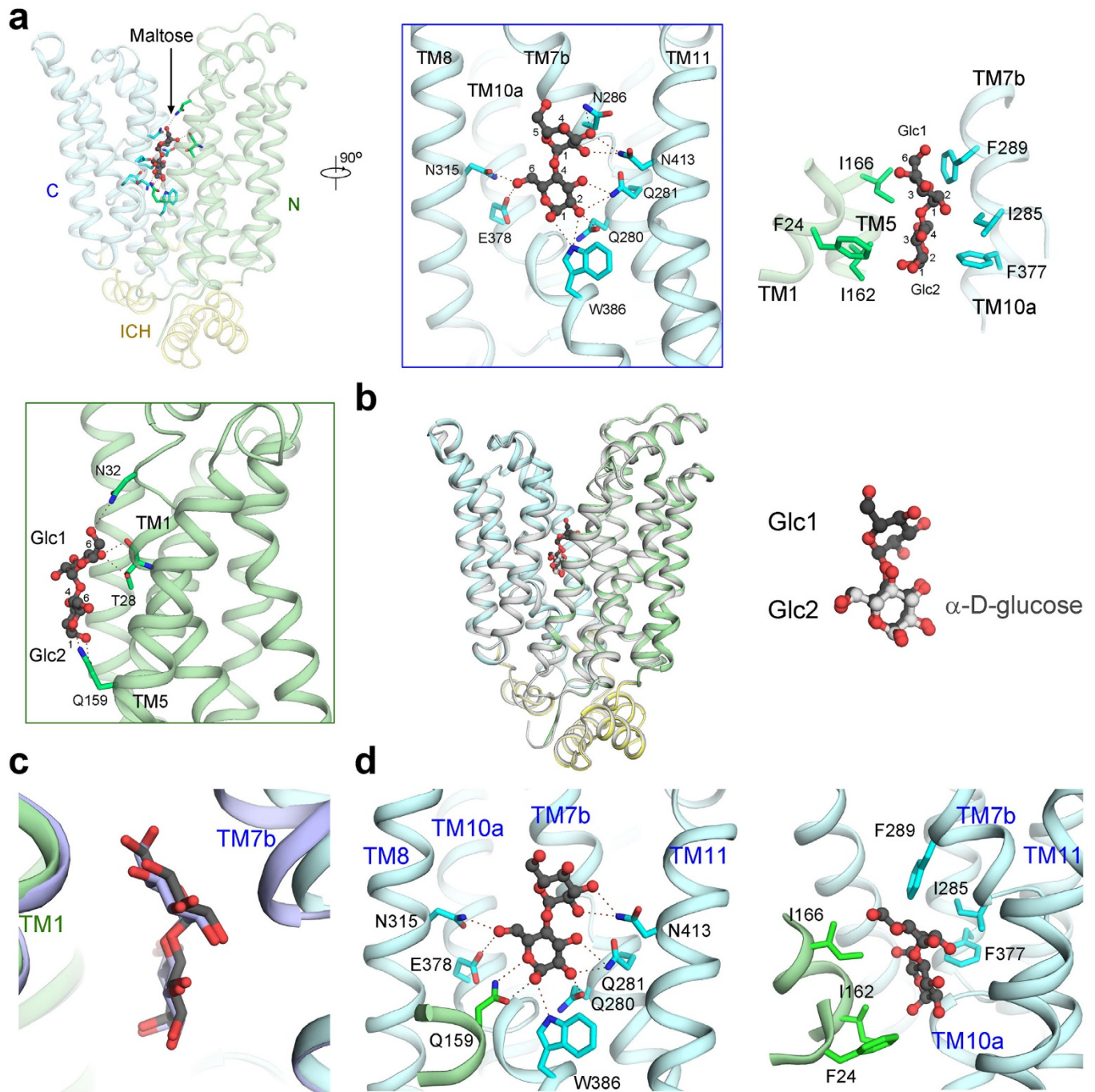
that may stabilize GLUTs in an outward-open conformation. The indicated disaccharides, where the C4-OH of D-glucose is condensed with another hexose, were tested for their abilities to inhibit glucose transport by GLUT1 or GLUT3 in the proteoliposome-based counterflow assay. Control refers to the conditions where no competitor was added.



Extended Data Figure 6 | Structure determination of GLUT3 in complex with maltose in the outward-open and outward-occluded conformations.

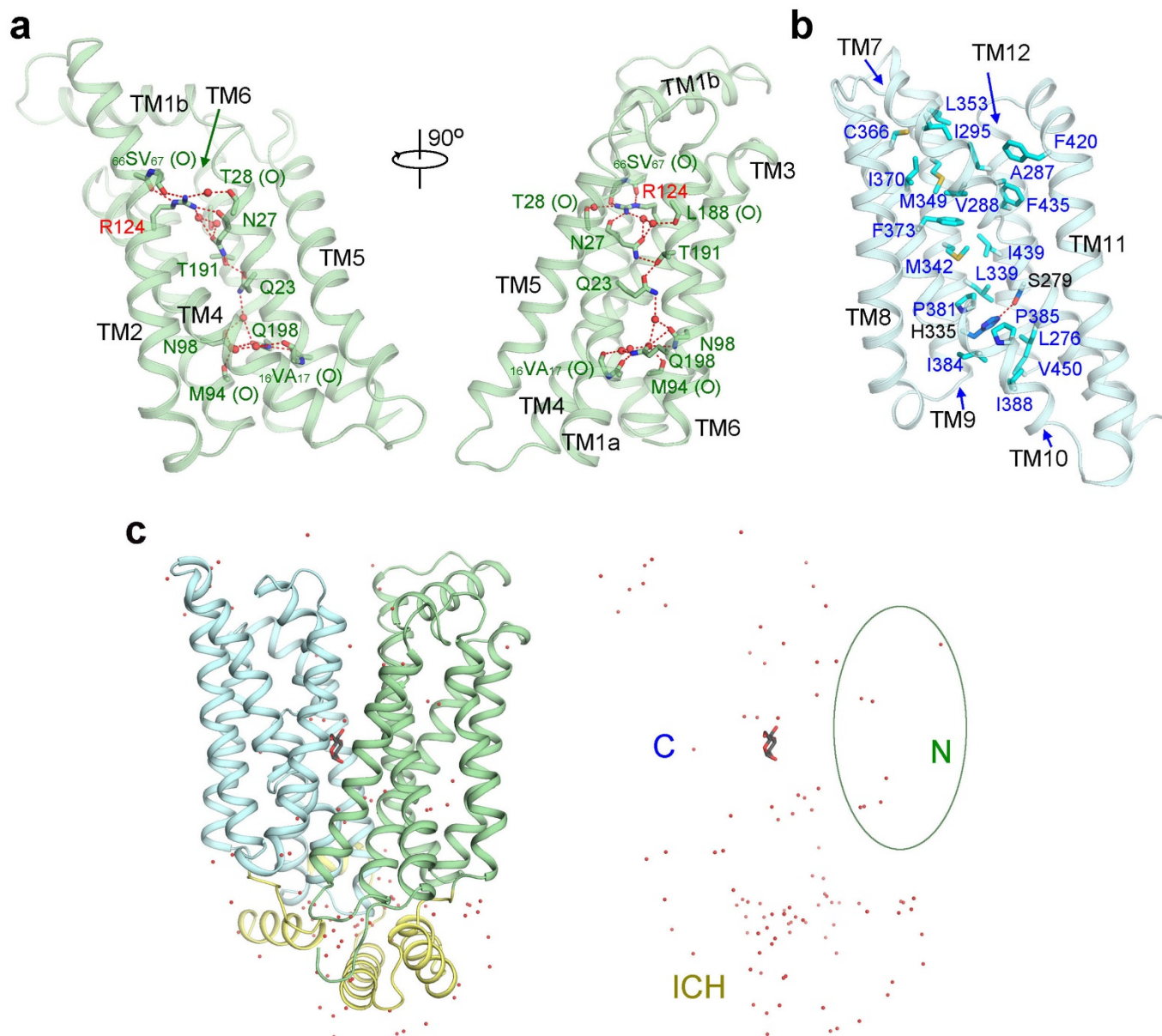
a, There are two GLUT3 molecules in each asymmetric unit of the outward-open structures. **b**, The crystal packing of the outward-open GLUT3. **c**, Structural superimposition of the two molecules in each asymmetric unit of the outward-open GLUT3. The two molecules exhibit nearly identical

conformations except for the extracellular loop regions. The focus was on molecule (Mol) A for structural analysis and comparison in the main text. **d**, The crystal packing of the outward-occluded GLUT3 bound to maltose. There is only one molecule in each asymmetric unit. **e**, **f**, The $2F_o - F_c$ electron density maps for the bound maltose in the outward-occluded (**e**) and outward-open (**f**) structures of GLUT3, both contoured at 1σ .



Extended Data Figure 7 | Maltose coordination in the outward-open and outward-occluded GLUT3. **a**, Coordination of maltose in the outward-occluded GLUT3 structure. Details of the polar interactions of maltose with residues from the N-terminal and C-terminal domains are shown in the insets on the bottom and right, respectively. Hydrogen bonds are represented by brown dashed lines. **b**, The structure of maltose-bound outward-occluded GLUT3 is nearly identical to that of the glucose-bound GLUT3. The second glucose unit (Glc2) of maltose completely overlaps with D-glucose, which is bound to the outward-occluded GLUT3. **c**, The bound maltose molecules are

positioned similarly in the outward-open and outward-occluded GLUT3. The two structures of GLUT3 are superimposed relative to the C-terminal domain. The outward-open GLUT3 is domain coloured and the outward-occluded structure is coloured pale purple. **d**, Maltose coordination in the outward-open GLUT3. Note that the coordination of Glc2 by the outward-open GLUT3 is identical to that by the outward-occluded GLUT3, while the polar residues in the N-terminal domain are not involved in the coordination of Glc1 in the outward-open structure.



Extended Data Figure 8 | The molecular basis underlying the rigidity and adaptability of the N-terminal and C-terminal domains, respectively.

a, Structural feature of the N-terminal domain of GLUT3. The interior of the N-terminal domain is held through a strip of hydrogen bonds, which may provide the molecular basis for the rigidity of the N-terminal domain during the alternating access cycle. **b**, The C-terminal domain of GLUT3 has a

hydrophobic core, which may allow the adaptability for the intra-domain shifts of the C-terminal domain during the transport cycle. **c**, Water distribution in the structure of glucose-bound GLUT3. The bound water molecules are shown as red spheres. Identical views are shown for the two panels except that the protein is omitted in the right panel to better illustrate the density of water molecules with respect to the N-terminal, C-terminal and ICH domains.

Extended Data Table 1 | Statistics of data collection and refinement of GLUT3 bound to D-glucose

Data	GLUT3/D-glucose
Integration Package	HKL2000
No. of crystals	1
Space Group	P2 ₁
Unit Cell (Å)	48.34, 118.13, 51.34
Unit Cell (°)	90, 102.67, 90
Wavelength (Å)	1.0000
Resolution (Å)	40~1.50 (1.55~1.50)
R _{merge} (%)	8.6 (57.8)
I/sigma	12.7 (3.6)
Completeness (%)	98.8 (91.8)
Number of measured reflections	444,895
Number of unique reflections	88,120
Redundancy	18.0 (2.0)
Wilson B factor (Å ²)	17.2
R _{work} / R _{free} (%)	17.53/19.42
No. atoms	
Protein	3,638
main chain	1,897
side chain	1,741
Substrate	12
Water	101
Others	75
Average B value (Å ²)	
Protein	25.08
main chain	22.93
side chain	27.43
Substrate	18.91
Water	40.50
Others	48.40
R.m.s. deviations	
Bonds (Å)	0.008
Angle (°)	1.095
Ramachandran plot statistics (%)	
Most favorable	97.0
Additionally allowed	3.0
Generously allowed	0.0
Disallowed	0.0

Extended Data Table 2 | Statistics of data collection and refinement of GLUT3 bound to maltose.

Data	Outward-occluded GLUT3/maltose	Outward-open GLUT3/maltose
Integration Package	HKL2000	HKL2000
No. of crystals	7	9
Space Group	P2 ₁	P2 ₁
Unit Cell (Å)	48.46, 119.49, 53.91	78.11, 121.88, 96.08
Unit Cell (°)	90, 103.75, 90	90, 108.14, 90
Wavelength (Å)	1.0000	1.0000
Resolution (Å)	40~2.40 (2.49~2.40)	40~2.60 (2.69~2.60)
R _{merge} (%)	13.0 (35.1)	14.3 (51.8)
I/sigma	12.7 (3.6)	10.5 (2.6)
Completeness (%)	94.6 (91.4)	95.0 (97.3)
Number of measured reflections	72,217	175,711
Number of unique reflections	22,422	49,602
Redundancy	3.2 (2.8)	3.5 (3.6)
Wilson B factor (Å ²)	33.3	84.6
R _{work} / R _{free} (%)	18.17 / 22.50	21.54 / 25.08
No. atoms		
Protein	3,593	7,186
main chain	1,872	3,744
side chain	1,721	3,442
Ligand	23	46
Water	36	52
Others	-	125
Average B value (Å ²)		
Protein	37.29	50.00
main chain	35.63	49.32
side chain	39.08	50.73
Ligand	38.24	59.00
Water	33.65	42.16
Others	-	60.8
R.m.s. deviations		
Bonds (Å)	0.009	0.010
Angle (°)	1.116	1.260
Ramachandran plot statistics (%)		
Most favourable	96.8	96.4
Additionally allowed	3.0	3.6
Generously allowed	0.2	0.0
Disallowed	0.0	0.0